In vivo molecular imaging for immunotherapy using ultra-bright near-infrared-IIb rare-earth nanoparticles

Yeteng Zhong[1,4], **Zhuoran Ma**[1,4], **Feifei Wang**[1,4], **Xi Wang**[2], **Yijun Yang**[2], **Yulai Liu**[1], **Xiang Zhao**[3], **Jiachen Li**[1], **Haotian Du**[1], **Mingxi Zhang**[1], **Qiuhong Cui**[2], **Shoujun Zhu**[1], **Qinchao Sun**[1], **Hao Wan**[1], **Ye Tian**[1], **Qiang Liu**[1], **Weizhi Wang**[1], **K. Christopher Garcia**[3], **Hongjie Dai**[1,*]

[1]Department of Chemistry and Bio-X, Stanford University, Stanford, California 94305, USA.

[2]Key Laboratory of Luminescence and Optical Information, Ministry of Education, Department of Physics, School of Science, Beijing Jiaotong University, Beijing 100044, P.R. China.

[3]Departments of Molecular and Cellular Physiology and Structural Biology, Stanford University School of Medicine, Stanford, California 94305, USA.

[4]These authors contribute equally to this work.

Abstract

The NIR-IIb (1500–1700 nm) window is ideal for deep-tissue optical imaging in mammals, but lacks bright and biocompatible probes. Here, we developed biocompatible cubic-phase (a-phase) erbium-based rare-earth nanoparticles (ErNPs) exhibiting bright downconversion luminescence at ~ 1600 nm for dynamic imaging of cancer immune-therapy in mice. We used ErNPs functionalized with cross-linked hydrophilic polymer layers attached to anti-PD-L1 antibody for molecular imaging of PD-L1 in a mouse model of colon cancer and achieved tumor to normal tissue signal ratios of ~ 40. The long luminescence lifetime of ErNPs (~ 4.6 ms) enabled simultaneous imaging of ErNPs and lead sulfide quantum dots (PbS QDs) emitting in the same ~ 1600 nm window. *In vivo* NIR-IIb molecular imaging of PD-L1 and CD8 revealed cytotoxic T lymphocytes in the tumor microenvironment in response to immunotherapy, and altered CD8 signals in tumor and spleen due to immune activation. The novel crosslinked functionalization layer facilitated 90% ErNPs excretion within two weeks without detectable toxicity in mice.

In recent years, *in vivo* fluorescence- and luminescence-based molecular imaging in the second near-infrared window (NIR-II, 1000–1700 nm) under ~ 800–1000 nm excitation have afforded high resolution imaging at sub-centimeter tissue depths benefiting from

suppressed photon scattering and diminished tissue autofluorescence in this spectral range. [1, 2] Several classes of NIR-II probes have been developed, including small molecules[3], carbon nanotubes (CNTs)[4], polymer encapsulated organic dyes[5], quantum dots[6], and rare-earth lanthanide ions (Ln^{3+}) doped nanoparticles[7]. Imaging at the long wavelength end of the NIR-II window (NIR-IIb, 1500–1700 nm) increases penetration depth to sub-centimeter and completely eliminate autofluorescence.[8–10] To date, CNTs[8], inorganic quantum dots (QDs), including lead sulfide (PbS)[9] and indium arsenide (InAs)[11], and erbium-doped hexagonal-phase (i.e. β-phase) rare-earth downconversion nanoparticles[12] have been developed as NIR-IIb probes for *in vivo* imaging. Nevertheless, the limited brightness of current NIR-IIb probes together with biocompatibility and toxicity concerns limit their potential for clinical translation.

Much excitement has been generated by immunotherapy based on immune checkpoint blockade of programmed cell death-1 (PD-1) and its ligand-1 (PD-L1) (herein, PD pathway) for cancer treatment.[13–17] Blocking the PD pathway with anti-PD-L1 (or anti-PD-1) monoclonal antibodies (mAb) can reverse cancer immune evasion and engender potent antitumor immunity in patients, resulted in durable cancer regression.[18–20] However, many challenges remain, including predicting patient therapeutic responsiveness and understanding how it is shaped by host and tumor components.[13, 21] Clinical and preclinical works to predict response to anti-PD therapy have been relying on *ex vivo* biopsy with immunohistochemistry (IHC)[22] and *in vivo* positron-emission tomography (PET)[23], single-photon emission computed tomography[24] and fluorescence imaging[25] to probe PD-L1 expression in tumor. An advantage of *in vivo* molecular imaging is the capability of dynamic monitoring and assessing PD-L1 heterogeneity in tumor. It is, however, important to maximize imaging sensitivity, signal to background ratios, spatial and temporal resolution, and penetration depth. Also, whereas PD-L1 expression in tumor is a useful biomarker; it is not the only predictor and should be combined with other cellular and molecular signatures of the tumor microenvironment to investigate therapeutic responses and mechanisms.[26–28] Among various modalities, optical molecular imaging allows for high spatial resolution at the micrometer scale[29], and possesses potential of performing multiplexed imaging to follow several molecular targets simultaneously[30, 31]. However, conventional optical molecular imaging based on fluorescence in the visible or near-infrared wavelengths < 900 nm has been superficial in penetration depth and unsatisfactory spatial resolution due to light-scattering and autofluorescence problems.[32, 33] PD-L1 molecular imaging has also been done using NIR-II fluorescence at ~ 1100 nm[25], affording a relatively high tumor to normal tissue ratio of ~ 9.5. Molecular imaging of PD-L1 in the long end of the NIR-II range (NIR-IIb, 1500–1700 nm) could further increase penetration depth to sub-centimeter and completely eliminate autofluorescence.[8–10]

Here, we report a novel Zn doped α-phase (i.e. cubic-phase; fluorite structure) rare-earth nanoparticle (ErNP) with a core-shell structure of $NaYbF_4$:2%Er,2%Ce,10%Zn@$NaYF_4$ (Fig. 1a). A ~ 11-fold enhancement of the downconversion luminescence over the previous brightest β-phase ErNPs[34] was achieved through enhancing multi-phonon relaxation in α-phase ErNPs over β-phase and reducing crystal field symmetry through Zn^{2+} ions doping. A hydrophilic polymeric crosslinked network was developed to impart aqueous solubility and biocompatibility to the ErNPs, allowing fast biliary excretion of intravenously administrated

nanoparticles within ~ 2 weeks without any discernable toxicity observed in mice. We also showed multiplexed molecular imaging in NIR-IIb using the ErNPs with milliseconds lifetime and our previously developed PbS QDs[9] with a much shorter microsecond lifetime, both emitting at ~ 1600 nm. Two-plex molecular imaging with anti-PD-L1 mAb labeled ErNPs (targeting PD-L1) and anti-CD8α mAb labeled PbS QDs (targeting CD8+ T cells) allowed *in vivo* noninvasive visualization of two molecular targets in the same NIR-IIb emission window.

Results

Cubic-phase *a*-ErNPs with vastly enhanced downconversion ~ 1550 nm luminescence

Thus far, erbium-based downconversion ErNPs were all in β-phase (hexagonal-phase)[7, 12, 34, 35] as an offspring of upconversion nanoparticles[36]. Earlier, we developed a β-phase ErNPs (NaYbF$_4$:Er,Ce@NaYF$_4$) with Ce doping to suppress upconversion and increase downconversion.[34] Here, we synthesized a different, *a*-phase (cubic-phase; fluorite structure) NaYbF$_4$:2%Er,2%Ce@NaYF$_4$ nanocrystal (*a*-ErNP; same structure with β-phase ErNPs) by tuning the temperature during co-thermolysis of rare-earth acetates in oleic acid and 1-octadecene (Supplementary Methods). In the cubic *a*-phase core, an Er^{3+} ion activator was surrounded by eight F$^-$ ions in the fluorite structure (Supplementary Fig. 1a). The core was encapsulated by epitaxial growth of a NaYF$_4$ inert shell to reduce the aqueous quenching effect.[34] The core-shell *a*-ErNPs were ~14 nm in size (Supplementary Fig. 1b), smaller than our previous β-phase ErNPs[34] (~ 18 nm). X-ray diffraction (XRD) (Supplementary Fig. 2) confirmed *a*-phase fluorite structure (JCPDS: 77–2043; space group: *Fm_3m*). Raman scattering result (Fig. 1b) corresponded to cubic-phase NaLnF$_4$ crystals, with phonon energies higher than those of β-phase.[37]

The downconversion NIR-IIb luminescence of *a*-ErNPs was about 7.6 times brighter than that of β-phase ErNPs upon 980 nm excitation (Fig. 1c). As shown in Figure. 1d, Yb^{3+} served as the sensitizer to harvest 980 nm photons. The activator Er^{3+} extracted the excitation energy from the Yb^{3+} through efficient cross-relaxation [(^{2}F$_{5/2}$)Yb, (^{4}I$_{15/2}$)Er] → [(^{2}F$_{7/2}$)Yb, (^{4}I$_{11/2}$)Er], populating the ^{4}I$_{11/2}$ state of Er^{3+}. Subsequent nonradiative relaxation of Er^{3+} ^{4}I$_{11/2}$ → ^{4}I$_{13/2}$ led to a population of ^{4}I$_{13/2}$ state, generating the 1550 nm downconversion NIR-IIb luminescence by radiative transition from ^{4}I$_{13/2}$ to the ground state ^{4}I$_{15/2}$. In the cubic *a*-phase, the ^{4}I$_{11/2}$ → ^{4}I$_{13/2}$ nonradiative transition by multiphonon orbit-lattice relaxation was enhanced over the hexagonal β-phase due to higher phonon energies (see Fig. 1b for Raman data) and Ln^{3+}-F$^-$ interaction strength in cubic-phase NaLnF$_4$ host lattice.[38] This led to a higher population of the ^{4}I$_{13/2}$ state and a 7.6-fold enhancement of the ^{4}I$_{13/2}$ → ^{4}I$_{15/2}$ downconversion 1550 nm luminescence over the brightest β-phase ErNPs (~18 nm) previously made[34].

Zn^{2+} doping enhances downconversion ~ 1550 nm luminescence brightness and lifetime

The luminescence intensity of free Ln^{3+} ions involved intra-4*f* electric-dipole transitions, which are parity-forbidden due to quantum mechanical selection rules. Such prohibition can be partially broken due to the mixing of opposite parity states when Ln^{3+} ions were embedded in crystal lattices; and a lower symmetry lattice can facilitate this mixing of

opposite parity configurations, resulting in luminescence enhancement of the rare earth ions.
[39] To enhance the downconversion luminescence, we doped Zn^{2+} ions (0.9 Å) into the a-ErNPs to make $NaYbF_4$:2%Er,2%Ce,10%Zn@$NaYF_4$ (Fig. 1a); and 10% Zn (nominal doping concentration) was found to be the optimal doping concentration (see Supplementary Table. 1 for practical concentration of Zn^{2+} ions), giving an 1.5 times higher downconversion luminescence in NIR-IIb than un-doped a-ErNPs (Fig. 1e). A total ~ 11-fold enhancement was achieved over the brightest β-phase ErNPs[34].

Energy dispersive X-ray (EDX) mapping of Zn doped a-ErNPs revealed uniform distribution of Zn^{2+} ions in the particles (Supplementary Fig. 3). XRD patterns of Zn doped a-ErNPs (Fig. 1f) showed (111) and (220) diffraction peaks shifting to larger 2θ values as Zn concentration increased (Supplementary Fig. 4a). This suggested shrinking of the unit cell when substituting the Ln^{3+} ions with smaller Zn^{2+} ions in the crystal lattice.[40] The doping of Zn^{2+} could be accompanied by generating a F^- vacancy, or occupy a Na^+ ion site and creating another Na^+ vacancy at the same time in order to maintain the charge balance (Supplementary Fig. 4b). As a result, the deformation of crystal lattice in the Zn doped a-ErNPs caused distortion of local symmetry around Er^{3+} ions, favoring 4f-4f transitions and the 1550 nm downconversion luminescence. Accordingly, the upconversion luminescence of Zn doped ErNPs was also enhanced by 0.33 times (Supplementary Fig. 4c). The absolute quantum yield (emission range: 1300–1800 nm) of the Zn doped ErNPs in aqueous solutions was estimated to be ~ 5% (Supplementary Fig. 4d) under the laser excitation of 100 mW/cm^2. Further increasing the Zn doping concentration might generate excessive distortions and defects, leading luminescence quenching (Fig. 1e).[41]

Importantly, the bright downconversion emission intensity of Zn doped cubic ErNPs was accompanied by a prolonged luminescence lifetime (Fig. 1g). For Zn doped a-ErNPs, the 1550 nm luminescence lifetime, i.e., the radiative part of the lifetime of the $^4I_{13/2}$ state of Er^{3+}, was measured to be ~ 7.0 ms (in cyclohexane) by time-resolved detection of emission from the particles. Such long-lived millisecond NIR-IIb luminescence of the ErNPs was useful for lifetime-based, time-resolved luminescence imaging, which can be utilized for multiplexed molecular imaging since luminescence with a longer lifetime can be easily distinguished from microsecond fluorescence of NIR-IIb PbS QDs.[42] Note that Zn doped a-ErNPs (named ErNPs in short) were used for all *vitro/vivo* experiments throughout this work.

Biocompatible, ultra-bright and excretable ErNPs for real-time NIR-IIb imaging

The bright 1550 nm luminescence of ErNPs is ideal for *in vivo* imaging; but such imaging hinges on imparting stability and biocompatibility to the ErNPs in aqueous and biological media without aggregation and associated toxicity. We devised hydrophilic, crosslinked coating layers on ErNPs (Fig. 2a) such that the probability of hydrophilic coating detaching from the particles was zero (see Method for detailed reactions). The crosslinked coating was composited of 4 polymer layers including an inner-most layer of hydrolyzed poly(maleic anhydride-*alt*-1-octadecene) (PMH) rich in -COOH groups, followed by an 8-arm branched polyethylene glycol amine (8Arm-PEG-NH_2) layer, a poly(acrylic acid) (PAA) layer and an outmost layer of mixed methoxy polyethylene glycol amine (mPEG-NH_2) and 8Arm-PEG-

NH_2 (in ~ 5:1 ratio, Supplementary Fig. 5). The multi-arm PEG-NH_2 stars and long PAA chains were responsible for crosslinking the polymeric layers. Dynamic light scattering (DLS) measurement showed an average hydrated size of ~ 35.5 nm in aqueous solution (Fig. 2b). On top of the PAA layer, the mixed mPEG-NH_2 and 8Arm-PEG-NH_2 outmost layer rendered the nanoparticles hydrophilic and water soluble, while imparting amine groups to allow conjugation of biological ligands for molecular imaging (Fig. 2a). The hydrophilic functionalized ErNPs showed remarkable stability in aqueous buffers (1xPBS) and serum without aggregation and exhibited zero photo-bleaching (Supplementary Fig. 6).

With the hydrophilic functionalized ErNPs intravenously injected into mouse, we performed noninvasive NIR-IIb imaging in real-time (defined as   30 frames-per-second, fps) to glean mouse cerebro-vasculatures (Supplementary video 1) through intact scalp/skull (Supplementary video 2). Owing to the highly bright ErNPs, real-time imaging was possible by using a low-power 970 nm LED lamp (15 mW/cm^2) as the excitation source. We clearly resolved cerebral blood flow variations over repeated cardiac cycles with high temporal and spatial resolution (Fig. 2c) using an excitation power ~ 10 times lower than laser based excitation sources used for previous rare-earth nanoparticles[34, 43]. Ventricular ejection phases (Fig. 2c) were resolved within 50 s post-injection (p.i.), compared to previous attempts in which cardiac cycle waveforms were only resolved ~ 5 s post-injection[2, 6]. Fast Fourier transformation (FFT) showed a clear heart beat frequency of 3.67 Hz, corresponding to the 276 ms interval between every two consecutive intensity spikes in Fig. 2c. Under a higher and safe excitation power, ultrafast NIR-IIb hindlimb vasculature imaging (Supplementary Fig. 7a; upon 980 nm diode laser excitation, 100 mW/cm^2) was carried out at a high frame rate of 90 fps (Supplementary video 3).

NIR-IIb imaging at ~ 1600 nm afforded deeper tissue penetration depths at sub-centimeter scale[8, 9], allowing for dynamic, noninvasive imaging of major organs and vasculatures *in vivo* (Supplementary Fig. 7b, c) for investigating the bio-distribution, pharmacokinetics and excretion of ErNPs tail-vein injected into mice (BALB/c; n = 3). Luminescence signals in liver and spleen gradually increased within 24 h p.i., suggesting accumulation of ErNPs from blood circulation into these organs (Fig. 2d; Supplementary Fig. 8c, d). Importantly, we observed strong luminescence signals of ErNPs in the feces of mice overtime (Supplementary Fig. 9b), indicating a biliary excretion pathway of ErNPs. Correspondingly, the signal intensity in the main organs of mice including liver and spleen kept decreasing within the monitored time period of 2 weeks (Fig. 2d, e). All of the feces excreted from mice were collected and measured by inductively coupled plasma optical emission spectrometry (ICP-OES), revealing that ~ 90% of injected a-ErNPs were excreted from the body in two weeks (Fig. 2f). This rapid, high degree excretion of ErNPs could facilitate clinical translation of the nanoparticles (see Supplementary Fig. 10 for histological studies).

ErNPs-anti PD-L1 mAb for *in vivo* molecular imaging and immunotherapy

In vivo fluorescence imaging under excitation < 1000 nm and emission in the ~ 1600 nm NIR-IIb window can benefit from greatly reduced photon scattering and an unusually large Stokes shift affording diminished autofluorescence/background interference.[9, 34] To investigate ErNPs as NIR-IIb probes targeting the PD-1/PD-L1 immune checkpoint, we

conjugated anti-PD-L1 mAb (Atezolizumab) to ErNPs ('ErNPs-aPDL1'; Supplementary Fig. 11e) with amine surface groups through 1-ethyl-3-(3-dimethylaminopropyl)carbodiimide (EDC) chemistry (see Method). Successful conjugation of anti-PD-L1 mAb to ErNPs was first confirmed by live cell imaging of CT-26 colon cancer cells (PD-L1 over-expressed) and 4T1 murine breast cancer cells (PD-L1 low-expressed) *in vitro* (Supplementary Fig. 12a).

In vivo molecular imaging of PD-L1 was done upon intravenous injection of ErNPs-aPDL1 into the tail vein of BALB/c mice (n = 5) bearing subcutaneous (s.c.) xenograft CT-26 tumors using a wide-field setup equipped with a 2D InGaAs camera by collecting emission photons between 1500–1700 nm under a 980 nm excitation at a power density of 50 mW/cm^2 (exposure time ~ 5 ms, Fig. 3a; Supplementary Fig. 13). About 200 μl of ErNPs-aPDL1 solution was intravenously injected, comprising of 250 μg anti-PD-L1 mAb (12.5 mg/kg) conjugated to ~ 2 mg ErNPs. The blood circulation time of $t_{1/2}$ ~ 5.5 h for ErNPs-aPDL1 in mice (Supplementary Fig. 14) was slightly longer than that of free ErNPs $t_{1/2}$ ~ 5.2 h (Supplementary Fig. 8b). The luminescence intensity inside CT-26 tumor increased steadily post injection, indicating extravasation of ErNPs-aPDL1 from blood circulation and enrichment in tumor.

The ErNPs-aPDL1 nanoparticles primarily accumulated in tumor, liver, spleen and intestine at 24 h p.i., with little retention in other organs including heart, lung, kidney and brain (Supplementary Fig. 15). The NIR-IIb signal ratio of tumor to normal tissues (T/NT) increased sharply during the initial hours post injection, and peaked at a T/NT ~ 42.2 ± 3.7 at 24 h p.i. (Fig. 3b). This T/NT ratio was remarkably high compared to previous fluorescence based molecular tumor imaging using fluorophores emitting in the entire optical range (T/NT ratios are typically ~ 2 – 4 in 700–900 nm NIR-I range[44, 45], and ~ 8 – 12 in the ~ 1100 nm NIR-IIa range[25, 32]). Without anti-PD-L1 mAb, the non-targeted free ErNPs showed much weaker signal in the CT-26 tumor (mice n = 3), with a lower peak T/NT ~ 11.0 ± 1.1 at 24 h p.i. (Fig. 3b) due to passive accumulation through the enhanced permeability and retention (EPR) effect. To further confirm specific *in vivo* targeting of ErNPs-aPDL1 to CT-26 tumor, we performed free anti-PD-L1 antibody blocking experiments (Supplementary Fig. 16) and observed much lower peak T/NT ~ 7.15 ± 0.55 at 24 h p.i., confirming highly specific ErNPs-aPDL1 targeting of CT-26 tumor. Importantly, the signal intensity of ErNPs-aPDL1 in the tumor mice liver and spleen kept decreasing within the monitored time period of 2 weeks (Supplementary Fig. 17a), similar to the free ErNPs in the healthy mice, indicating the fast excretion of intravenously administrated ErNPs-aPDL1 from tumor mice. The aspartate/alanine aminotransferases (AST/ALT) measurements also demonstrated no discernable toxicity of ErNPs-aPDL1 *in vivo* (Supplementary Fig. 17b).

Next, we imaged BALB/c mice bearing s.c. murine breast 4T1 tumors (mice n = 3) with low PD-L1 expression using the same intravenously injected ErNPs-aPDL1 (Fig. 3a). The peak T/NT ratio reached 12.3 ± 1.2 at 24 h p.i. (Fig. 3b), much lower than T/NT ~ 42 for ErNPs-aPDL1 injected mice bearing CT-26 tumor, which was consistent with *ex vivo* tumor PD-L1 expression analysis based on flow cytometry (Supplementary Fig. 12b). The high T/NT ratio of > 40 with the ErNPs-aPDL1 probe for CT-26 tumor was resulted from combined effects

of high specificity of ErNPs-aPDL1 toward PD-L1 immune checkpoint, the vastly boosted luminescence brightness of Zn-doped cubic-phase a-ErNP NIR-IIb probes, and near-zero autofluorescence of biological tissues under a large ~ 600 nm Stokes shift from 980 nm excitation to ~ 1600 nm emission.

We reduced the amount of anti-PD-L1 mAb by an order of magnitude (from 250 μg to 20 μg mAb), conjugated to the same 2 mg of ErNPs (ErNPs-1/10[th]aPDL1) for each ~ 200 μl injection (antibody dose ~ 1 mg/kg) and still obtained excellent result of molecular imaging of PD-L1 in tumors (mice n = 3; Fig. 3c). The peak T/NT ratio was 31.1 ± 2.1 at 24 h p.i. for CT-26 tumors on BALB/c mice (Fig. 3b). Molecular imaging using low doses of PD-L1 antibody (therapeutic doses were up to ~ 10–20 mg/kg in the clinic)[20–22] would be preferred for therapeutic response assessment due to lower cost and, more importantly reduced potential side-effect risks[46, 47]. When zooming into the tumor (Fig. 3d), we imaged noninvasively through the skin to glean ErNPs-aPDL1 NIR-IIb signals circulating in the tortuous tumor vasculature at 5 min p.i., resolving vessels in CT-26 tumor down to micrometer spatial resolution. Leakage of ErNPs-aPDL1 from blood vessels into tumor tissue was also observed (Fig. 3d), indicating the start of ErNPs-aPDL1 extravasation and binding to cancer cells within the tumor. Interestingly, we observed that anti-PD-L1 mAb conjugated to ErNP surfaces retained the PD-1/PD-L1 checkpoint blocking capability of free antibodies for therapeutic cancer treatment (see Figure 3e, 3f; Supplementary Fig. 18–20), suggesting ErNPs-aPDL1 as a theranostic agent for both molecular PD-L1 imaging and immunotherapy.

Two-plex *in vivo* molecular imaging at ~ 1600 nm for PD-L1 markers and CD8+ cytotoxic T lymphocytes

Activated CD8+ cytotoxic T lymphocytes (CTLs) in response to antibody treatment play critical roles in immune checkpoint blockade therapy by infiltrating into tumor and inducing apoptosis of cancer cells.[46] *In vivo* imaging and evaluating the bio-distribution of CTLs in relation to PD-L1 expression could provide insights into activation and migration of T cells in response to antibody immunotherapeutic treatment. To this end we developed a novel two-plex NIR-IIb molecular imaging approach to simultaneously mapping out CD8+ CTL and PD-L1 *in vivo*.

Exploiting the long-lived ~ 1550 nm luminescence (4.3 ms in aqueous solution) of ErNPs, we devised time-resolved imaging to differentiate ErNP luminescence from short-lived fluorescence of QDs for two-plex molecular imaging in the same 1500–1700 nm NIR-IIb window (Fig. 4a, b). Our recently developed PbS QDs[9] exhibited shorter-lived 1600 nm fluorescence with a lifetime of ~ 46 μs (Fig. 4c) and were combined with ErNPs as the second NIR-IIb imaging probe. For imaging PbS emission without ErNP luminescence (Fig. 4a), we used 808 nm continuous-wave (CW) laser for excitation that was absorbed only by PbS QDs (Fig. 4d, e) and not by ErNPs (absorption in ~ 900–1000 nm range; Fig. 4d). For imaging ErNP luminescence without PbS emission (Fig. 4b), we used 980 nm pulse (pulse duration ~ 1 ms) for excitation and set a delay time of 1 ms to the InGaAs CCD camera through computer-control to allow full fading of the short-lived fluorescence (46 μs) of PbS QDs before recording. Subsequent recording with the camera collected the 1550 nm long-

lived luminescence (4.3 ms) signals from ErNPs, affording a distinct ErNPs detecting channel (Fig. 4b) without any PbS fluorescence.

To track the CD8+ T cells *in vivo*, we conjugated anti-CD8α mAb (clone 2.43) to PbS QDs (PbS-aCD8) for targeting CD8+ CTLs. BALB/c mice (n = 3) bearing CT-26 s.c. tumors were intravenously injected with a mixture of ErNPs-aPDL1 and PbS-aCD8 (Fig. 4f). We first performed *in vivo* 360° rotation imaging of mouse whole-body to glean the bio-distribution of ErNPs-aPDL1 and PbS-aCD8 in tumor, liver, spleen and other organs at 24 h p.i. (Fig. 4g; Supplementary video 4). Strong signal in CT-26 tumor appeared in the ErNPs channel (green, Fig. 4f, g) due to targeting of ErNPs-aPDL1. Meanwhile we also observed accumulation of PbS-aCD8 labeled CD8+ T cells within the tumor in the PbS channel (red, Fig. 4f, g). When zoomed into the tumor for high-magnification imaging, the shape of CT-26 tumor was clearly visualized in ErNPs channel with a relatively even signal distribution through the tumor (Supplementary Fig. 21). While for the PbS-aCD8 channel, the signals were higher around the periphery of the tumor and extending inward (see Fig. 4f; Supplementary Fig. 21b and Supplementary Fig. 22b), a result consistent with *ex vivo* analysis by flow cytometry (Supplementary Fig. 22c–e). This suggested the infiltration of immune-competent CD8+ CTLs starting primarily from the periphery region of the CT-26 tumor, and was limited by vascular hyper-permeability and shortage of functional lymphatic vessels inside solid tumors.[48]

To confirm specific *in vivo* targeting of PbS-aCD8 to CD8+ CTLs in CT-26 tumor, we performed CD8 blocking experiments (Fig. 5a). BALB/c mice (n = 3) bearing CT-26 tumors were first tail-vein injected with ErNPs-aPDL1 and free anti-CD8α mAb (same dose as to the antibody on the PbS-aCD8). At 48 h p.i., the ErNPs-aPDL1 accumulated in CT-26 tumors with consistently high T/NT ratio of ~ 40.1 (Fig. 5b). Then, PbS-aCD8 were intravenously injected at 48 h post co-injection of ErNPs-aPDL1 and free anti-CD8 mAb. Strong signal from PbS-aCD8 was only detected in the liver and spleen at 24 h post the second injection (Fig. 5a, b), with little signal of PbS-aCD8 in the CT-26 tumor. This suggested blocking of CD8α receptors on the T cells from the first injection of free anti-CD8 mAb, validating the specificity of PbS-aCD8 towards CD8+ T cells. The PbS-aCD8 nanoparticles (in healthy mice) primarily accumulated in liver, spleen and intestine at 24 h p.i., with little retention in other organs including heart, lung, kidney and brain (Supplementary Fig. 23).

We observed that for CT-26 tumors on mice that received both PbS-aCD8 and anti-PD-L1 treatment (with ErNP-aPDL1), accumulation of PbS-aCD8 in the tumor was high and weak in main organs including liver and spleen (Fig. 5c), suggesting the clonally expanded activated effector T cells in spleen trafficking to and infiltrating the tumor bed, and killing the cancer cells (Fig. 3e).[46] Contrary to this immune activated group with good response to immunotherapy, mice (n = 3) bearing CT-26 tumor injected with PbS-aCD8 alone without any PD-L1 antibody blockade treatment (Fig. 5d; Supplementary video 5) showed prominent PbS-aCD8 signals in the liver and spleen (spleen signal/background ~ 19.3 vs. ~ 2.1 in the immune activated case; Supplementary Fig. 24a, b), with a lower PbS-aCD8 signal T/NT ratio of ~ 6.5 (Supplementary Fig. 24b) than immune activated mice treated by PD-L1 blockade therapy (PbS-aCD8 signal T/NT ratio ≈ 10.2; Supplementary Fig. 24a). This was

consistent with *ex vivo* flow cytometry results (Supplementary Fig. 25). Further, for 4T1 tumor bearing mice (n = 3) injected with ErNPs-aPDL1 and PbS-aCD8 (Fig. 5e; Supplementary video 6) and 4T1 tumor bearing mice (n = 3) injected with free ErNPs and PbS-aCD8 (Supplementary Fig. 26), no therapeutic response/tumor regression was observed and CD8+ T cells were primarily in the liver and spleen, similar to the case of mice bearing CT-26 tumor without any anti-PD-L1 treatment or immune activation.

Analysis of *in vivo* rotating NIR-IIb images recorded at various angles allowed plotting of CD8+ T cell signal ratio between tumor and spleen (T/spleen) for analysis of immune system activation and responses to immunotherapy (Fig. 5f). We found that the (T/spleen)_CD8 ratio of ~ 5.3 in immune activated, ErNPs-aPDL1 treated CT-26 bearing mice was > 15 times higher than (T/spleen)_CD8 ratio of CT-26 mice without anti-PD-L1 treatment [(T/spleen)_CD8 ratio ~ 0.31], and > 30 times higher than (T/spleen)_CD8 ratio of 4T1 mice treated by anti-PD-L1 but without responses [(T/spleen)_CD8 ratio ~ 0.14]. The result suggested that a robust immune response to antibody treatment involved a large proportion of CTLs activated and migrating from lymphoid organs rich in immune cells (e.g., spleen) into tumor to eradicate cancer cells (see Supplementary Fig. 18 for therapeutic effect). Thus, noninvasive *in vivo* two-plex NIR-IIb imaging to glean tumor PD-L1 level and CD8+ T cell distribution in tumor vs. spleen could provide useful parameters for assessing response to immunotherapy. We note that the bio-distribution and expression level of a single biomarker can be properly evaluated based on NIR-II signals of the nanoparticles; while the parallel quantification of two biomarkers based on the duplex signals from two nanoparticles could be affected by the difference in the nanoparticle extravasation into the tumor and may be subject to less accuracy.

Discussion

While upconversion nanoparticles have been investigated for decades, downconversion luminescence of erbium-doped ErNPs at ~ 1600 nm for *in vivo* NIR-II imaging with sub-centimeter tissue penetration and micrometer image resolution was only recent.[12, 31, 34] This work developed the first ultra-bright cubic-phase ErNPs for noninvasive NIR-IIb imaging of biomarkers important to immunotherapy. These rare-earth nanoparticles are of low-toxicity[49, 50] without toxic element such as Pb, Cd and Hg. Also important to biocompatibility is the hydrophilic coating on ErNP formed by crosslinking polymeric layers, forming a capping network to prevent detachment of the coating. The ~ 90% biliary excretion of intravenously administrated ErNPs from mice in 2 weeks alleviates concerns of long-term toxicity due to retention. It is therefore potentially possible to use ErNP-aPDL1 for humans in the clinic, for *in vivo* assessment of PD-L1 status in tumors that are near the body surface such as melanoma, head and neck cancer or other cancers through endoscopy techniques. Lifetime imaging using the ErNPs is exciting in terms of combining with other novel probes to image multiple immune targets in the same NIR-IIb window simultaneously with molecular specificity.

Checkpoint blockade cancer immunotherapy involves antibody blocking of the checkpoint inhibitor PD-L1 on tumor cells, activation of the immune system and tumor infiltration of immune-competent T lymphocytes.[13] Currently clinical *in vitro* IHC diagnostic assays rely

on biopsy to analyze tumor cell PD-L1 expression status and presence/proportion of tumor-infiltrating immune cells for predicting patients' likelihood of positive response to immunotherapy. *In vivo* molecular imaging by techniques such as PET can address the issue of PD-L1 distribution inhomogeneity.[23, 45] However, no technique has been developed thus far for *in vivo* probing of two or more important immune elements simultaneously.

Combining ~ 1600 nm emitting ErNPs and PbS quantum dots, our two-plex molecular imaging revealed heterogeneous bio-distributions of PD-L1 and CD8+ CTLs. We observed high T/NT ratios of PD-L1 in CT-26 colon tumors with favorable therapeutic responses to anti-PD-L1 therapy and much lower T/NT of PD-L1 in non-responding 4T1 tumors. For mice bearing CT-26 tumors without antibody therapy or non-responding 4T1 tumors with antibody treatment, (T/spleen)_CD8 ratio is low with a high proportion of CD8+ immune cells in lymphoid tissues. For CT-26 tumor treated by anti-PD-L1 mAb, potent antitumor immunity was generated accompanied by the observation of high (T/spleen)_CD8 ratios, indicating the vast majority of activated CTLs accumulating in tumor to recognize and eradicate the tumor. A low (T/spleen)_CD8 ratio observed under co-administration of anti-PD-L1 and a CD8 probe could be an indicator for ineffective blockade of PD-1/PD-L1 signaling mediated tumor immunity dysfunction. Such *in vivo* noninvasive bio-distribution assessments of tumor cells and immune cells in the whole body could complement *ex vivo* biopsy-based diagnostic methods. Thus, it is possible to develop a specific scoring algorithm combining *in vivo* tumor PD-L1 expression level and immune cells status to provide a more accurate prediction for immunotherapeutic response.

Online Methods

Reagents

Rare-earth(III) acetate hydrate (RE: Yb, Er, Ce), zinc acetate, sodium trifluoroacetate, oleic acid (OA), 1-octadecene (ODE), sodium hydroxide, ammonium fluoride, 1-(3-dimethylaminopropyl)-3-ethylcarbodiimide hydrochloride (EDC), Poly(acrylic acid) (PAA; average Mw 1800), poly(maleic anhydride-*alt*-1-octadecene) (PMH; 30–50 kDa), 4-morpholineethanesulfonic acid (MES), 4-(dimethylamino)pyridine (DMAP), cyclohexane, chloroform, 2-Amino-2-(hydroxymethyl)-1,3-propanediol (tris-base), fetal bovine serum (FBS), phosphate buffered saline (PBS), and RPMI-1640 medium were purchased from Sigma-Aldrich and used without further purification. Yttrium(III) oxides and trifluoroacetic acid (99%) were purchased from Alfa Asea and used as received. Methoxy polyethylene glycol amine (mPEG-NH$_2$; 5000 m.W.) was purchased from Laysan-Bio. 8-arm polyethylene glycol amine (8Arm-PEG-NH$_2$; 40 kDa) was purchased from Advanced Biochemicals. Anti-PD-L1 monoclonal antibody (Atezolizumab, Clone SP142) was purchased from Selleckchem. Anti-CD8α monoclonal antibody (Clone 2.43) was purchased from Bio X Cell. EZ-Link™ Sulfo-NHS-LC-Biotin and DRAQ5 Fluorescent Probe were purchased from Thermo Fisher Scientific. Streptavidin was purchased from ProSpec. Y(CF$_3$COO)$_3$ was prepared by the literature method.[51] Detailed information on the antibodies is included in the Life Sciences Reporting Summary.

Synthesis of a-NaYbF$_4$:Ce,Er,Zn (core) nanoparticles

In a typical synthetic procedure of a-NaYbF$_4$:Ce,Er,Zn, 0.075 mmol of Zn(CH$_3$COO)$_2$ and 0.75 mmol of RE(CH$_3$COO)$_3$ (RE: 96% Yb, 2% Ce, 2% Er) were added to a mixture of OA (15 mmol), ODE (37.5 mmol) in a two-necked flask at room temperature. The solution was heated to 150 °C for 30 minutes under argon gas flow with vigorous magnetic stirring before cooling down to 50 °C. Then NaOH (75 mg) and NH$_4$F (111 mg) dissolved in methanol (8 ml) were added into above solution, and kept at 50 °C for 1 hour under argon gas flow with vigorous magnetic stirring. Then the solution was heated to 100 °C under argon gas protection, and degassed for 10 minutes before being heated to 295 °C. The solution was maintained at 295 °C for 1 hour and heated to 300 °C for another 20 minutes. After cooling to room temperature, an excess amount of ethanol was poured into the solution. The resultant nanocrystals were centrifuged at 4400 rpm for 30 minutes, washed with ethanol several times, and dispersed in 3 ml of cyclohexane for further coating. Note that, the synthesis of a-NaYbF$_4$:Ce,Er (without Zn doping) was the same as above procedure except that Zn(CH$_3$COO)$_2$ was not needed for the synthesis.

Synthesis of a-NaYbF$_4$:Ce,Er,Zn@NaYF$_4$ (core-shell) nanoparticles

In a typical two-step synthetic procedure of a-NaYbF$_4$:Ce,Er,Zn@NaYF$_4$ (or a-NaYbF$_4$:Ce,Er@NaYF$_4$ without Zn doping), an amount of 1 mmol CF$_3$COONa, 1 mmol Y(CF$_3$COO)$_3$ and the as-prepared core nanoparticles were added to a mixture of OA (20 mmol), ODE (20 mmol) in a two-necked flask at room temperature. The solution was pre-degassed for 30 minutes with vigorous magnetic stirring then heated to 120 °C under vacuum for 30 minutes to remove water and oxygen. The solution was then heated to 295 °C for 75 minutes and 300 °C for another 20 minutes under argon protection. After cooling to room temperature, an excess amount of ethanol was poured into the solution. The resultant nanoparticles were centrifuged at 4400 rpm for 30 minutes, washed with ethanol several times, and dispersed in 3 ml of cyclohexane. Above synthetic procedure was repeated again with the same reagents and temperature to afford the final a-NaYbF$_4$:Ce,Er,Zn@NaYF$_4$ core-shell nanoparticles, dispersed in 3 ml of cyclohexane (the mass concentration was ~ 80 mg/ml).

Surface modification of ErNPs with crosslinked polymer network

PMH [80 mg; poly(maleic anhydride-*alt*-1-octadecene); 30–50 kDa] was dissolved in 5 ml chloroform in 10 ml flask. Then ErNPs (32 mg) dispersed in cyclohexane was added. The solution was stirred for 1 hour and then rotary evaporated for 30 minutes to remove the organic solvent. The residual was kept at 60 °C oven for overnight to remove excess organic solvent. Then DMAP [80 mg; 4-(dimethylamino)pyridine] dissolved in 6 ml water solution was added. The flask was sonicated until the ErNPs were fully dispersed. Above solution was centrifuged at 14000 rpm for 2 hours for 2 times to remove the excess PMH and DMAP. The sediment was resuspended in 3 ml MES (4-morpholineethanesulfonic acid) solution (10 mM, pH = 8.5). Then 8Arm-PEG-NH$_2$ (12 mg; 8-arm polyethylene glycol amine) dissolved in 3 ml MES solution was added. EDC [8 mg; 1-(3-dimethylaminopropyl)-3-ethylcarbodiimide hydrochloride] was added then. The solution was shaken to react for 3 hours. Tris-base [40 mg; 2-Amino-2-(hydroxymethyl)-1,3-propanediol] and then EDC (20

mg) dissolved in MES solution were added into above solution to block the excess -COOH group derived from PMH. The solution was reacted for another 3 hours, and then centrifuged at 4400 rpm for 30 minutes to remove potential large floccules. The supernate was dialyzed against water for 12 hours (300 kDa; change water for more than 8 times) to fully remove excess PEG and de-active the EDC. Then the solution was washed by centrifugal filter (100 kDa) for 1 time, and then dispersed in 3 ml MES solution. PAA [4 mg; Poly(acrylic acid)] dissolved in 3 ml MES solution was added to above solution. EDC (8 mg) dissolved in MES solution was added then. The solution was shaken for 1 hour (longer reaction time will cause a large amount of floccules) before centrifuged at 4400 rpm for 30 minutes to remove potential large floccules. The supernate was washed by centrifugal filter (100 kDa) for 4 times to remove excess PAA, and then dispersed in 3 ml MES solution. mPEG-NH$_2$ (4 mg; methoxy polyethylene glycol amine) and 8Arm-PEG-NH$_2$ (0.8 mg) dissolved in 3 ml MES solution were added. Then EDC (8 mg) dissolved in MES solution was added, and the solution was shaken for 3 hours. Tris-base (20 mg) and then EDC (10 mg) dissolved in MES solution were added into above solution to block the excess -COOH group derived from PAA. The solution was shaken for another 3 hours before centrifuged at 4400 rpm for 30 minutes to remove potential large floccules. The supernate was washed by centrifugal filter (100 kDa) for 4 times to remove excess PEG. The final ErNPs (~ 16 mg) with crosslinked polymer network were dispersed in 1.6 ml 1xPBS solution at 4 °C for long-term storing.

Conjugation of anti-PD-L1 mAb on ErNPs (ErNPs-aPDL1)

Above ErNPs store solution (200 μl, containing 2 mg ErNPs), anti-PD-L1 mAb (250 μg), EDC (1.5 mg) and 800 μl MES solution (10 mM, pH = 8.5) were mixed and shaken for 3 hours. The solution was centrifuged at 4400 rpm for 30 minutes to remove potential large floccules. The supernate was washed by centrifugal filter (100 kDa) for 2 times, and then dispersed in 200 μl 1xPBS solution (for one injection).

Conjugation of anti-CD8α mAb on PbS QDs (PbS-aCD8)

The water-dispersible PbS QDs were prepared by our previously developed method.[52] PbS QDs (0.25 mg) in 50 μl 1xPBS solution, EDC (0.75 mg) and streptavidin (50 μg) were added to 500 μl MES solution (10 mM, pH = 6.5). The solution was stirred at room temperature for 3 hours, and then washed by centrifugal filter (100 kDa) for 4 times to obtain PbS-streptavidin (dispersed in 100 μl 1xPBS solution). On the other hand, anti-CD8α mAb (150 μg) was dissolved in 300 μl 1xPBS solution. Then 6 μl EZ-Link™ Sulfo-NHS-LC-Biotin (1.7 mg/ml in DMSO) was added. The solution was stirred at room temperature for 1.5 hours, and then washed by centrifugal filter (100 kDa) for 4 times to obtain anti-CD8α mAb-biotin (dispersed in 100 μl 1xPBS solution). Above as-prepared PbS-streptavidin and anti-CD8α mAb-biotin were mixed, and stirred at room temperature for 2 hours. The solution was washed by centrifugal filter (100 kDa) for 2 times, and then dispersed in 200 μl 1xPBS solution (for one injection).

Mouse handling

All vertebrate animal experiments were performed under the approval of the Stanford University's Administrative Panel on Laboratory Animal Care. All experiments were

performed in accordance with the National Institutes of Health Guide for the Care and Use of Laboratory Animals. BALB/c female mice were purchased from Charles River. The surrounding relative humidity level was 55–65% and the temperature was ~ 25 °C. The hair of mice was carefully removed using Nair to avoid causing wounds to the skin. Before NIR-IIb *in vivo* imaging, a rodent anaesthesia machine with 2 L/minute O_2 gas flow mixed with 2.5% isoflurane was used to anaesthetize the mice. During the dynamic imaging, the mouse was kept anaesthetized by a nose cone delivering 2 L/minute O_2 gas mixed with 2.5% isoflurane. For *in vivo* dynamic imaging (real-time and ultrafast), an 1xPBS solution of ErNPs (40 mg/ml, 200 μl) was injected. Mice were randomly selected from cages for all experiments. All groups within study contained n = 3–5 mice. CT-26 tumors were generated by subcutaneous injection of 2×10^6 CT-26 cells in 50 μl PBS. 4T1 tumors were generated by subcutaneous injection of 2×10^6 4T1 cells in 50 μl PBS. The mice were used for imaging and treatment when the volume of the tumor reached 20 mm^3 (about 3 days post inoculation).

Dynamic fluorescence imaging in the NIR-IIb window

A water-cooled, 640×512 pixel two-dimensional InGaAs array (detecting range: 400–1700 nm; Raptor Photonics) was used to carry out *in vivo* imaging of mouse brain and hindlimb. For light-emitting diode (LED) excited real-time *in vivo* imaging of mouse cerebral vessels, the excitation light was provided by a 970 nm LED lamp (100 W) equipped with an aluminum heatsink cooling fan and a 60 degree lens. The excitation power density at the imaging plane was 15 mW/cm^2. The emitted luminescence was allowed to pass through a 1100 nm and a 1500 nm long-pass filter (Thorlabs) to ensure the NIR images taken in the NIR-IIb region of 1500–1700 nm. The upper bound at 1700 nm was determined by the sensitivity profile of the InGaAs detector. A lens pair consisting of two achromats (200 mm and 100 mm; Thorlabs) was used to focus the image onto the detector with a field of view of 25 mm × 20 mm. The exposure time for each image acquisition was 23.3 ms, while the overhead time of the camera is 10 ms. Therefore, the frame rate we used for real-time imaging is 1 / (23.3 ms + 10 ms) = 30 Hz (or 30 frames per second). For ultrafast *in vivo* imaging of mouse hindlimb vessels, the excitation light was provided by a 980 nm continuous-wave (CW) laser coupled to a collimator (F240SMA-980; Thorlabs). The excitation power density at the imaging plane was 100 mW/cm^2. The imaging setup is the same as above. The exposure time for each image acquisition was 1.11 ms, thus the frame rate we used for ultrafast imaging is 1 / (1.11 ms + 10 ms) = 90 Hz.

Optical emission spectrometry (ICP-OES) measurement

Tissue and feces samples were digested in concentrated nitric acid (68%) for overnight, followed by heating in concentrated nitric acid and hydrogen peroxide for 2 hours using a hot plate, to obtain clear solutions. The Yb contents in the solutions were determined by ICP-OES (Thermo Scientific ICAP 6300 Duo View Spectrometer), and the Yb contents in the mice tissues and feces were subsequently calculated.

Lifetime measurement

The lifetime measurement was performed on a microscope mounted with an 100X (NA = 0.8) objective to focus the 980 nm laser. 980 nm excitation and fluorescence signal were

separated by a dichroic mirror with cut-off wavelength of 980 nm. After collected by the 100X objective, the fluorescence signal was focused by a 200 mm tube lens, filtered by a 1500 nm long-pass filter and transmitted to an InGaAs photomultiplier tube (PMT, H12397–75, Hamamatsu) through a multimode fiber. Fluorescence signal recording was realized by synchronously controlling the PMT and a 980 nm laser using Labview software through a data acquisition card (NI USB-6210). The fluorescence signal was immediately recorded by the PMT 1 ms after excitation was turned off.

Two-plex molecular imaging in the NIR-IIb window

A water-cooled, 640×512 pixel two-dimensional InGaAs array (detecting range: 400–1700 nm, Ninox 640, Raptor Photonics) was used to carry out *in vivo* two-plex imaging of tumor bearing mice. A lens pair consisting of two achromats (200 mm and 75 mm; Thorlabs) was used to focus the image onto the detector with a field of view of 65 mm × 50 mm. For PbS channel, the excitation light was provided by an 808 nm diode laser with CW model and filtered by two short-pass filters with cutoff wavelengths at 850 nm and 1000 nm. The excitation power density at the imaging plane was 50 mW/cm^2. The emitted luminescence was allowed to pass through a 1100 nm and a 1500 nm long-pass filter (Thorlabs) to ensure the NIR images taken in the NIR-IIb region of 1500–1700 nm. The exposure time for each image acquisition was 20 ms. For ErNPs channel, the excitation light was provided by a 980 nm diode laser at modulation model to generate laser pulse (duration: 1 ms, peak power density: 50 mW/cm^2). In the lifetime-resolved imaging system, synchronous control of the camera and laser was realized using Labview software through a data acquisition card (NI USB-6210). First an 1-ms laser pulse was triggered to excite the nanoparticles, then wait another 1 ms, then a luminescence image with exposure time of 5 ms was captured by the camera. The emitted luminescence was allowed to pass through a 1100 nm and a 1500 nm long-pass filter (Thorlabs) to ensure the NIR images taken in the NIR-IIb region of 1500–1700 nm. For high-magnification two-plex molecular imaging in the NIR-IIb window, the lens pair was changed to an optical lens system (Optem Zoom 70XL) to provide a field of view of 1.2 mm × 1 mm.

High-magnification molecular imaging in the NIR-IIb window

A water-cooled, 640×512 pixel two-dimensional InGaAs array (detecting range: 400–1700 nm; Raptor Photonics) equipped with an optical lens system (Optem Zoom 70XL) was used to carry out high-magnification molecular imaging. The emitted NIR-IIb signal was allowed to pass through a 1100 nm and a 1500 nm long-pass filter (Thorlabs) to ensure the NIR images taken in the NIR-IIb region of 1500–1700 nm. The high-magnification molecular imaging with the maximum magnification provided a view field of 1.2 mm × 1 mm.

In vitro profiling of PD-L1

CT-26 cancer cells (high PD-L1 expression), 4T1 cancer cells (low PD-L1 expression), and HEK293 human cells (no PD-L1 expression) were seeded at a number of 1×10^4 per well in chambered slides as three groups with 400 μl RPMI-1640 cell media. After cells were incubated in a humidified atmosphere of 5% CO^2 at 37 °C for 12 hours, the cells were washed twice with 400 μl cold 1xPBS buffer (4 °C). ErNPs-aPDL1 were subsequently added into each group, respectively, at the same dose and interacted with the cells for 30 minutes at

4 °C, followed by twice wash with cold PBS buffer. The cells were then fixed with 4% paraformaldehyde for 30 minutes at room temperature and nucleus were stained using 100 μl DRAQ5 (1×10^{-6} M). In the end, the fixed cells were imaged under a home-built NIR-II microscope with both NIR-I and NIR-II channels.

Flow cytometry

For harvesting cells from the CT-26 and 4T1 tumor, the tumor was dissected out, cut into small pieces. The tumor tissues were dissociated using the Miltenyi mouse tumor dissociation kit according to the manufacturers' instructions. The preparations were passed through a 70 μm cell strainer and washed thoroughly with PBS buffer supplemented with 0.5% BSA (PBS-BSA buffer). Finally, the cells were resuspended in PBS-BSA buffer and stained with CD8 alpha Monoclonal Antibody (KT15). FITC (for CD8+ T cells) or CD274 (PD-L1, B7-H1) Monoclonal Antibody (MIH5), Super Bright 780, eBioscience™ (for PD-L1 expression levels) for flow cytometry on Beckman Coulter CytoFLEX flow cytometer and analyzed using FlowJo. For harvesting cells from spleen tissues, the spleen was minced finely with scissors and scalpel, and mashed on a 70 μm cell strainer to create a single-cell suspension. The red blood cells were lysed by incubating cells in ACK lysis buffer for 10 minutes and mononuclear cells were washed thoroughly with PBS-BSA buffer. Finally, the cells were resuspended in PBS-BSA buffer and stained with CD8 alpha Monoclonal Antibody (KT15). FITC (for CD8+ T cells) for flow cytometry on Beckman Coulter CytoFLEX flow cytometer and analyzed using FlowJo.

Absolute quantum yield measurement

The absolute quantum yield measurement was performed by following a literature protocol[53] with slight modifications. The NIR-IIb probes were excited by a 980 nm laser (for Zn doped α-ErNPs and β-ErNPs) or an 808 nm laser (for PbS quantum dots). The laser power density was 100 mW/cm^2. An integrating sphere (Thorlabs; IS200) was used to spread the incoming light by multiple reflections over the entire sphere surface. The outcome lights, including laser excitation light and NIR fluorescence of NIR-IIb probes, were taken using a home-built NIR spectroscopy with a spectrometer (Acton SP2300i) equipped with a liquid-nitrogen cooled InGaAs linear array detector (Princeton OMA-V). Note that, the excitation light has to be attenuated by a neutral density filter (Newport; OD = 2.0) before being detected. According to the equation (1), the absolute quantum yield of NIR-IIb probes was calculated.

$$\text{QY} = \frac{photons\ emitted}{photons\ absorbed} = \frac{E[\text{sample}]}{L[\text{blank}] - L[\text{sample}]} \tag{1}$$

Where QY is the quantum yield, E[sample] is the emission intensity, L[blank] and L[sample] are the intensities of the excitation light in the presence of the water and the NIR-IIb probe sample, respectively.

Statistics and data analysis

Data analysis was performed in Origin 9.0.0. Means ± SD were calculated by Origin 9.0.0. In Fig. 3b and Fig. 5b, background was measured from a randomly selected area without

vasculatures or tumors. T/NT is the ratio of fluorescence signals in the whole tumors area over the randomly selected background. For each representative experimental result, the number of successful independent experiments performed is indicated in the corresponding figure legend.

Characterization

Transmission electron microscopy (TEM) images were taken with a JEM-2100F transmission electron microscope (JEOL) operating at 200 kV. Energy dispersive X-ray (EDX) mapping images were obtained on a JEM-2100F equipped with an energy dispersive X-ray analyzer. Inductively coupled plasma optical emission spectrometry (ICP-OES) were performed on a Thermo Scientific ICAP 6300 Duo View Spectrometer. Dynamic light scattering (DLS) and zeta potential measurements were performed on a Malvern Zetasizer Nano ZS90. X-ray diffraction (XRD) patterns were recorded on a Philips XPert PRO MPD X-ray diffractometer operated at 35 kV and 45 mA with Cu-Kα radiation. The upconversion luminescent properties were studied using a Horiba Jobin Yvon FluoroLog3 spectrometer equipped with a 980 nm diode laser as excitation. The downconversion luminescent properties were studied using an Acton SP2300i spectrometer equipped with an InGaAs linear array detector (Princetion OMA-V) and using a 980 nm diode laser as excitation. NIR fluorescence images of the downconversion emission were obtained using 2D InGaAs array (Ninox 640, Raptor Photonics) with 640×512 pixel using a 980 nm diode laser as excitation. Raman spectra were obtained with polarized incident laser light (λ = 532 nm) on Jobin Yvon T64000.

Reporting Summary

Further information on research design is available in the Nature Research Reporting Summary linked to this article.

Data availability

The data that support the findings of this study are available from the corresponding author upon reasonable request.

Supplementary Material

Refer to Web version on PubMed Central for supplementary material.

Acknowledgements

References

1. Hong G et al. Through-skull fluorescence imaging of the brain in a new near-infrared window. Nat. Photonics 8, 723–730 (2014). [PubMed: 27642366]

2. Antaris AL et al. A high quantum yield molecule-protein complex fluorophore for near-infrared II imaging. Nat. Commun 8, 15269 (2017). [PubMed: 28524850]

3. Yang Q et al. Donor engineering for NIR-II molecular fluorophores with enhanced fluorescent performance. J. Am. Chem. Soc 140, 1715–1724 (2018). [PubMed: 29337545]

4. Liu Z et al. In vivo biodistribution and highly efficient tumour targeting of carbon nanotubes in mice. Nat. Nanotech 2, 47–52 (2006).

5. Wan H et al. A bright organic NIR-II nanofluorophore for three-dimensional imaging into biological tissues. Nat. Commun 9, 1171 (2018). [PubMed: 29563581]

6. Bruns OT et al. Next-generation in vivo optical imaging with short-wave infrared quantum dots. Nat. Biomed. Eng 1, 0056 (2017). [PubMed: 29119058]

7. Naczynski DJ et al. Rare-earth-doped biological composites as in vivo shortwave infrared reporters. Nat. Commun 4, 2199 (2013). [PubMed: 23873342]

8. Diao S et al. Fluorescence imaging in vivo at wavelengths beyond 1500 nm. Angew. Chem 127, 14971–14975 (2015).

9. Zhang M et al. Bright quantum dots emitting at ~1,600 nm in the NIR-IIb window for deep tissue fluorescence imaging. Proc. Natl. Acad. Sci 115, 6590–6595 (2018). [PubMed: 29891702]

10. Diao S et al. Biological imaging without autofluorescence in the second near-infrared region. Nano Res. 8, 3027–3034 (2015).

11. Franke D et al. Continuous injection synthesis of indium arsenide quantum dots emissive in the short-wavelength infrared. Nat. Commun 7, 12749 (2016). [PubMed: 27834371]

12. Shao W et al. Tunable narrow band emissions from dye-sensitized core/shell/shell nanocrystals in the second near-infrared biological window. J. Am. Chem. Soc 138, 16192–16195 (2016). [PubMed: 27935695]

13. Zou W, Wolchok JD, Chen L PD-L1 (B7-H1) and PD-1 pathway blockade for cancer therapy: mechanisms, response biomarkers, and combinations. Sci. Transl. Med 8, 328rv4 (2016).

14. Okazaki T et al. A rheostat for immune responses: the unique properties of PD-1 and their advantages for clinical application. Nat. Immunol 14, 1212–1218 (2013). [PubMed: 24240160]

15. Sheng W et al. LSD1 ablation stimulates anti-tumor immunity and enables checkpoint blockade. Cell 174, 549–563.e519 (2018). [PubMed: 29937226]

16. Butte MJ et al. Programmed death-1 ligand 1 interacts specifically with the B7–1 costimulatory molecule to inhibit T cell responses. Immunity 27, 111–122 (2007). [PubMed: 17629517]

17. Hu Q et al. Conjugation of haematopoietic stem cells and platelets decorated with anti-PD-1 antibodies augments anti-leukaemia efficacy. Nat. Biomed. Eng 2, 831–840 (2018). [PubMed: 31015615]

18. Powles T et al. MPDL3280A (anti-PD-L1) treatment leads to clinical activity in metastatic bladder cancer. Nature 515, 558–562 (2014). [PubMed: 25428503]

19. Sagiv-Barfi I et al. Therapeutic antitumor immunity by checkpoint blockade is enhanced by ibrutinib, an inhibitor of both BTK and ITK. Proc. Natl. Acad. Sci 112, E966–E972 (2015). [PubMed: 25730880]

20. Lau J et al. Tumour and host cell PD-L1 is required to mediate suppression of anti-tumour immunity in mice. Nat. Commun 8, 14572 (2017). [PubMed: 28220772]

21. Bensch F et al. 89Zr-atezolizumab imaging as a non-invasive approach to assess clinical response to PD-L1 blockade in cancer. Nat. Med 24, 1852–1858 (2018). [PubMed: 30478423]

22. Herbst RS et al. Predictive correlates of response to the anti-PD-L1 antibody MPDL3280A in cancer patients. Nature 515, 563–567 (2014). [PubMed: 25428504]

23. Mall S et al. Immuno-PET imaging of engineered human T cells in tumors. Cancer Res. 76, 4113–4123 (2016). [PubMed: 27354381]

24. Nedrow JR et al. Imaging of programmed cell death ligand 1: impact of protein concentration on distribution of anti-PD-L1 SPECT agents in an immunocompetent murine model of melanoma. J. Nucl. Med 58, 1560–1566 (2017). [PubMed: 28522738]

25. Wan H et al. Developing a bright NIR-II fluorophore with fast renal excretion and its application in molecular imaging of immune checkpoint PD-L1. Adv. Funct. Mater 28, 1804956 (2018).

26. Balar AV et al. Atezolizumab as first-line treatment in cisplatin-ineligible patients with locally advanced and metastatic urothelial carcinoma: a single-arm, multicentre, phase 2 trial. Lancet 389, 67–76 (2017). [PubMed: 27939400]

27. Daud AI et al. Programmed death-ligand 1 expression and response to the anti-programmed death 1 antibody pembrolizumab in melanoma. J. Clin. Oncol 34, 4102–4109 (2016). [PubMed: 27863197]

28. Shen X, Zhao B Efficacy of PD-1 or PD-L1 inhibitors and PD-L1 expression status in cancer: meta-analysis. BMJ 362, k3529 (2018). [PubMed: 30201790]

29. Hong G et al. Multifunctional in vivo vascular imaging using near-infrared II fluorescence. Nat. Med 18, 1841–1846 (2012). [PubMed: 23160236]

30. Zhu S et al. Molecular imaging of biological systems with a clickable dye in the broad 800- to 1,700-nm near-infrared window. Proc. Natl. Acad. Sci 114, 962–967 (2017). [PubMed: 28096386]

31. Fan Y et al. Lifetime-engineered NIR-II nanoparticles unlock multiplexed in vivo imaging. Nat. Nanotech 13, 941–946 (2018).

32. Wang W et al. Molecular cancer imaging in the second near-infrared window using a renal-excreted NIR-II fluorophore-peptide probe. Adv. Mater 30, 1800106 (2018).

33. Antaris AL et al. A small-molecule dye for NIR-II imaging. Nat. Mater 15, 235–242 (2015). [PubMed: 26595119]

34. Zhong Y et al. Boosting the down-shifting luminescence of rare-earth nanocrystals for biological imaging beyond 1500 nm. Nat. Commun 8, 737 (2017). [PubMed: 28963467]

35. Wang R, Li X, Zhou L, Zhang F Epitaxial seeded growth of rare-earth nanocrystals with efficient 800 nm near-infrared to 1525 nm short-wavelength infrared downconversion photoluminescence for in vivo bioimaging. Angew. Chem. Int. Ed 53, 12086–12090 (2014).

36. Wang F et al. Simultaneous phase and size control of upconversion nanocrystals through lanthanide doping. Nature 463, 1061–1065 (2010). [PubMed: 20182508]

37. Klier DT, Kumke MU Analysing the effect of the crystal structure on upconversion luminescence in Yb^{3+},Er^{3+}-co-doped $NaYF_4$ nanomaterials. J. Mater. Chem. C 3, 11228–11238 (2015).

38. Sommerdijk JL Influence of host lattice on the infrared-excited visible luminescence in Yb^{3+}, Er^{3+}-doped fluorides. J. Lumin 6, 61–67 (1973).

39. Chen G et al. Upconversion emission enhancement in Yb^{3+}/Er^{3+}-codoped Y_2O_3 nanocrystals by tridoping with Li^+ ions. J. Phys. Chem. C 112, 12030–12036 (2008).

40. Li D et al. Efficient luminescence enhancement of Gd2O3:Ln3+ (Ln = Yb/Er, Eu) NCs by codoping Zn2+ and Li+ inert ions. Opt. Mater. Express 7, 329–340 (2017).

41. Yu AK et al. Luminescence of rare-earth ions and intrinsic defects in Gd_2O_3 matrix. J. Phys. Conf. Series 741, 012089 (2016).

42. Lu Y et al. Tunable lifetime multiplexing using luminescent nanocrystals. Nat. Photonics 8, 32–36 (2013).

43. Dang X et al. Layer-by-layer assembled fluorescent probes in the second near-infrared window for systemic delivery and detection of ovarian cancer. Proc. Natl. Acad. Sci 113, 5179–5184 (2016). [PubMed: 27114520]

44. Chatterjee S et al. A humanized antibody for imaging immune checkpoint ligand PD-L1 expression in tumors. Oncotarget 7, 10215–10227 (2016). [PubMed: 26848870]

45. Chatterjee S, Lesniak WG, Nimmagadda S Noninvasive imaging of immune checkpoint ligand PD-L1 in tumors and metastases for guiding immunotherapy. Mol. Imaging 16, 1 (2017).

46. Seidel JA, Otsuka A, Kabashima K Anti-PD-1 and anti-CTLA-4 therapies in cancer: mechanisms of action, efficacy, and limitations. Front. Oncol 8, 86 (2018). [PubMed: 29644214]

47. Brahmer JR et al. Safety and activity of anti-PD-L1 antibody in patients with advanced cancer. N. Engl. J. Med 366, 2455–2465 (2012). [PubMed: 22658128]

48. Jain RK, Stylianopoulos T Delivering nanomedicine to solid tumors. Nat. Rev. Clin. Oncol 7, 653–664 (2010). [PubMed: 20838415]

49. Liu C, Hou Y, Gao M Are rare-earth nanoparticles suitable for in vivo applications? Adv. Mater 26, 6922–6932 (2014). [PubMed: 24616057]

50. Wang X et al. Single ultrasmall Mn2+-doped NaNdF4 nanocrystals as multimodal nanoprobes for magnetic resonance and second near-infrared fluorescence imaging. Nano Res. 11, 1069–1081 (2018).

Methods-only References

51. Mai H-X et al. High-quality sodium rare-earth fluoride nanocrystals: controlled synthesis and optical properties. J. Am. Chem. Soc 128, 6426–6436 (2006). [PubMed: 16683808]

52. Ma Z et al. Near-infrared IIb fluorescence imaging of vascular regeneration with dynamic tissue perfusion measurement and high spatial resolution. Adv. Funct. Mater 28, 1803417 (2018). [PubMed: 31327961]

53. Boyer J-C & van Veggel FCJM Absolute quantum yield measurements of colloidal NaYF4: Er3+, Yb3+ upconverting nanoparticles. Nanoscale 2, 1417–1419 (2010). [PubMed: 20820726]
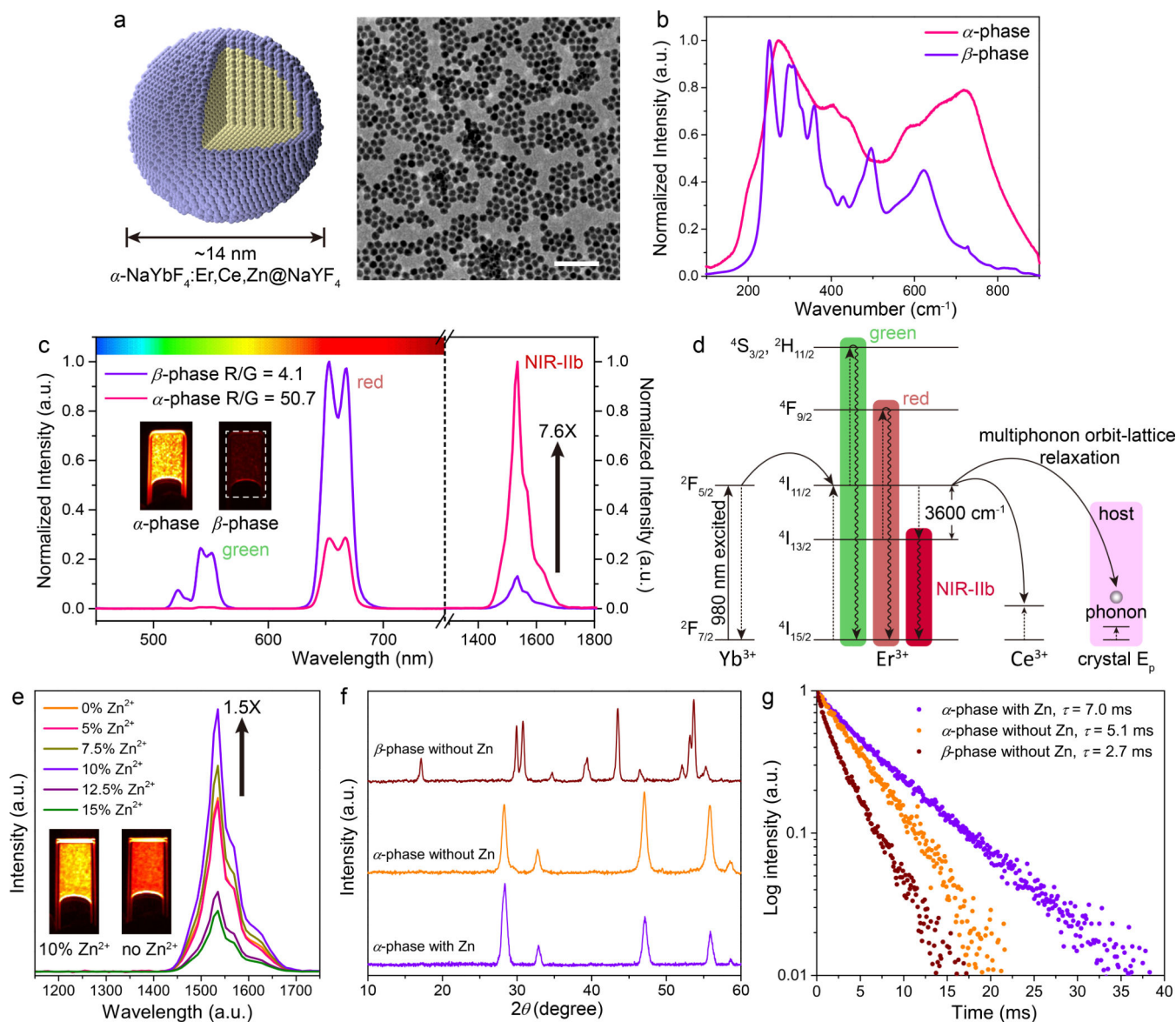
Figure 1: Ultra-bright ~ 1550 nm NIR-IIb luminescence of Zn doped a-ErNPs.
a, Schematic design of core-shell Zn doped a-ErNPs (left) and corresponding large scale TEM image (right, scale bar = 100 nm). **b,** Raman spectra of cubic-phase a-ErNPs and our previously reported hexagonal-phase ErNPs[34]. **c,** Upconversion and downconversion luminescence spectra of a-ErNPs and β-phase ErNPs. The insets showed NIR-IIb luminescence images of these two nanoparticles in cyclohexane. **d,** Simplified energy-level diagrams depicting the energy transfer involved in a-ErNPs upon 980 nm excitation. **e,** Downconversion luminescence spectra of Zn doped a-ErNPs with different Zn^{2+} concentration (0%, 5%, 7.5%, 10%, 12.5% and 15%, nominal doping concentration). The insets showed NIR-IIb luminescence images of a-ErNPs with 10% and 0% Zn^{2+} doping. **f, g,** XRD patterns **f** and lifetime decays **g** of cubic-phase a-ErNPs (10% Zn doping), cubic-phase a-ErNPs (0% Zn doping), and β-phase ErNPs. Similar results for n > 3 independent experiments.
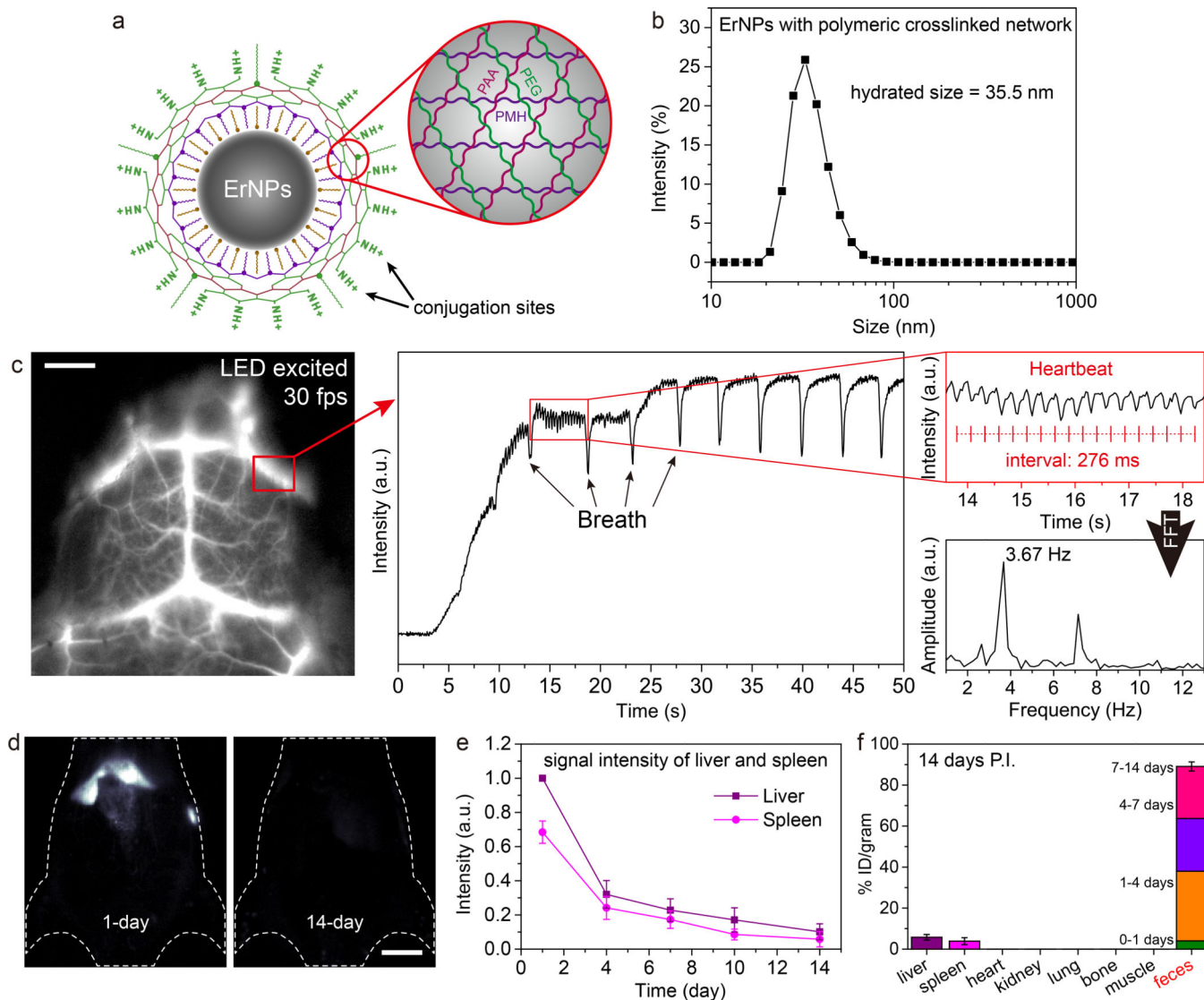
Figure 2: Biocompatible, rapid excretable *a*-ErNPs for real-time NIR-IIb imaging under low power light emitting diode (LED) excitation.

a, Schematic illustration of the hydrophilic ErNPs with crosslinking polymeric layers and amine groups on the surface as conjugation sites. **b,** DLS spectra of hydrophilic ErNPs with polymeric crosslinked network. **c,** NIR-IIb cerebral vascular image (left) by intravenous injection of 200 μl ErNPs (40 mg/ml) and excited by a 970 nm LED (30 fps). The luminescence intensity of an inferior cerebral vein was plotted as a function of time (middle), showing the cardiac cycles (upper right) with a heartbeat frequency of 3.67 Hz by FFT (lower right). Scale bar: 5 mm. **d,** The wide-field images showed the ErNPs luminescence signal in liver and spleen at 1-day and 14-day p.i. Scale bar: 1 cm. **e,** The excretion of ErNPs from the mice (n = 3) liver and spleen can be seen by plotting the signal intensity in these organs (normalized to liver signal observed on 1 day p.i.) as a function of time within 2 weeks. **f,** Bio-distribution of ErNPs in main organs and feces of ErNPs-treated mice (n = 3) at 14 days p.i. All data are presented as means ± s.d. Similar results for n > 3 independent experiments.
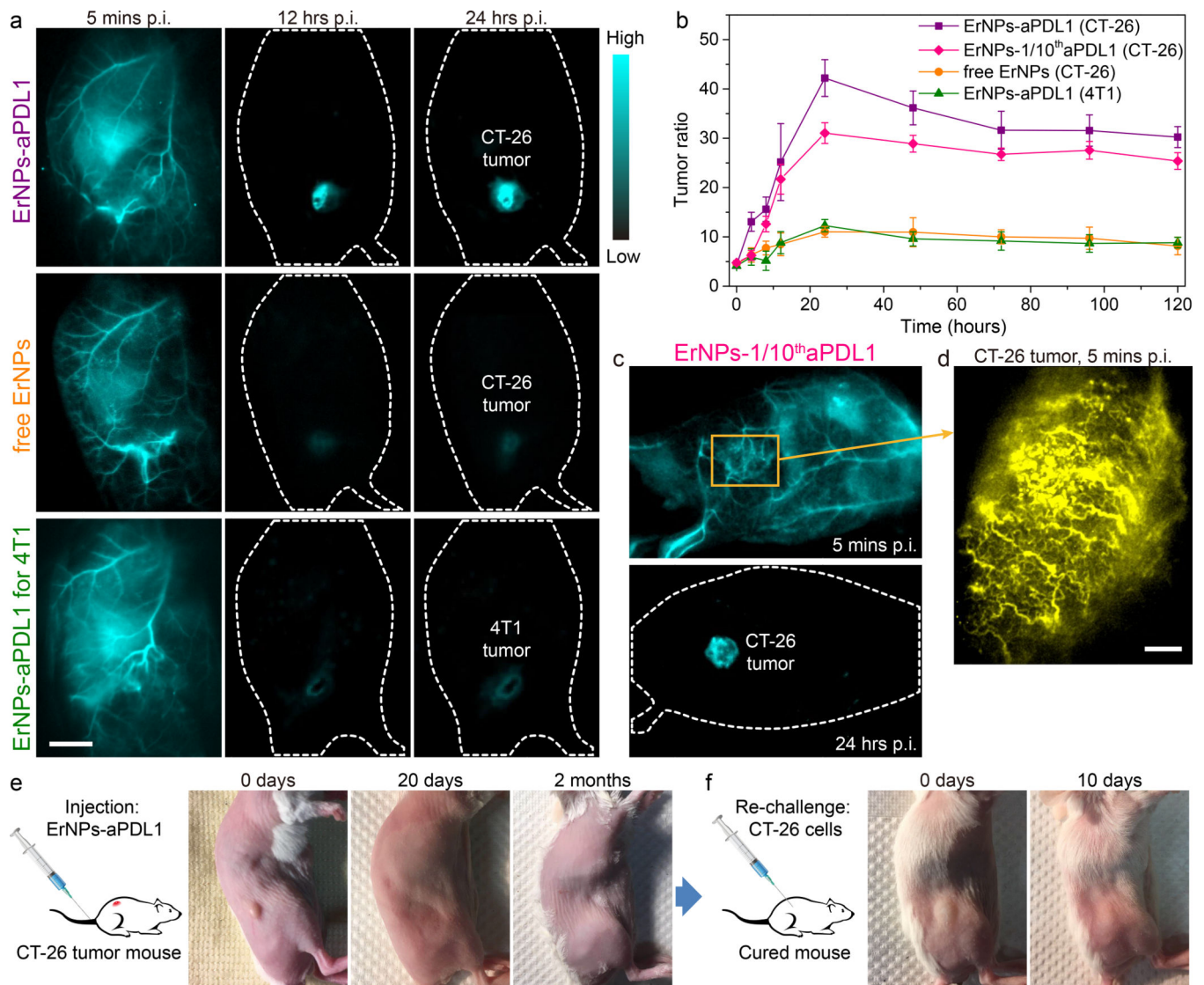
Figure 3: ErNPs-anti-PD-L1 mAb complex for *in vivo* PD-L1 molecular imaging and immunotherapy.

a, The wide-field images of CT-26 tumor mice (n = 5) treated with ErNPs-aPDL1 (upper), CT-26 tumor mice (n = 3) treated with free ErNPs (middle), and 4T1 tumor mice (n = 3) treated with ErNPs-aPDL1 (lower) at different time points p.i. (5 mins, 12 hrs, and 24 hrs). Scale bar: 1 cm. **b,** The T/NT ratio of ErNPs in tumor were plotted as a function of time within 120 hours. **c,** The wide-field images of a CT-26 tumor mouse treated with ErNPs-1/10th aPDL1 containing 20 μg anti-PD-L1 mAb (1 mg/kg). **d,** High-magnification molecular imaging of the CT-26 tumor at 5 minutes post injection of ErNPs-1/10th aPDL1 (scale bar: 500 μm). **e,** Photographs of a CT-26 tumor mouse treated with ErNPs-aPDL1 at 0 days, 20 days, and 2 months post intravenous injection of ErNPs-aPDL1. **f,** Photographs of a cured mouse s.c. inoculated with 2×10^6 CT-26 cells at 0 days and 10 days post inoculation. All data are presented as means ± s.d. Similar results for n > 3 independent experiments.
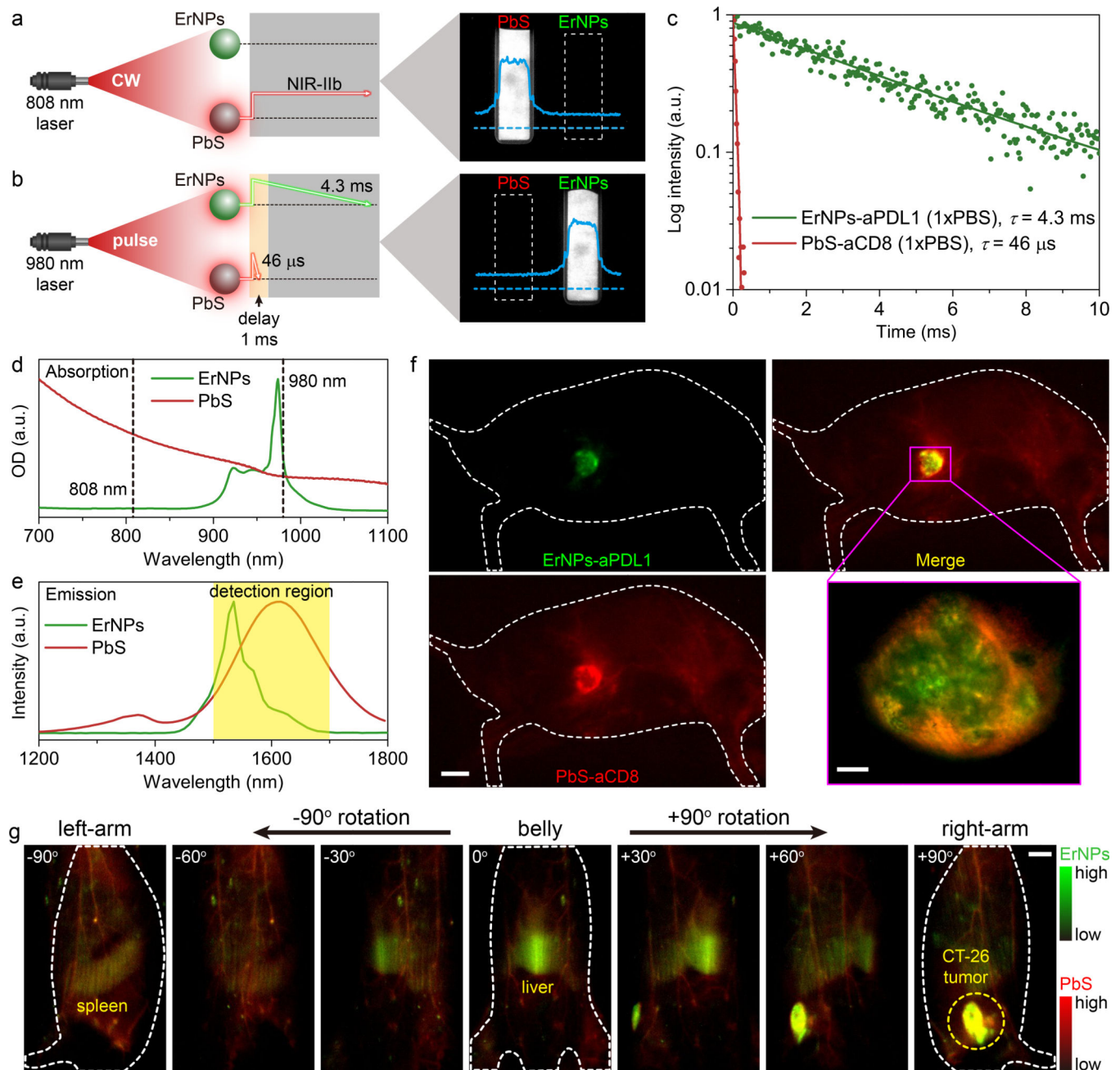
Figure 4: *In vivo* two-plex NIR-IIb molecular imaging of immune responses using ErNPs-aPDL1 and PbS-aCD8 at the same ~1600 nm emission range.

a, Schematic illustration outlining the experimental setup (left) to distinguish the PbS QDs emission channel (right) by using an 808 nm CW laser. **b,** Schematic of the experimental setup (left) to differentiate the long-lived ErNPs luminescence (right) from short-lived PbS QDs fluorescence by using a 980 nm laser pulse. The insets showed corresponding cross-sectional intensity profiles (blue color). **c,** Lifetime decays of ErNPs-aPDL1 and PbS-aCD8 in phosphate buffered saline solution (1xPBS). **d,** Absorption spectra of ErNPs-aPDL1 and PbS-aCD8. **e,** Emission spectra of ErNPs-aPDL1 and PbS-aCD8. The detection region is 1500–1700 nm. **f,** Two-plex molecular imaging (upper right) of a CT-26 tumor mouse at 24

hrs post intravenous injection of mixed ErNPs-aPDL1 (green color, upper left) and PbS-aCD8 (red color, lower left). Scale bar: 5 mm. The zoomed-in high-magnification two-plex image (lower right) outlined the CT-26 tumor with micrometer image resolution (scale bar: 500 μm). **g,** Corresponding two-plex rotation (−90° to +90°) imaging showed the *in vivo* bio-distribution of ErNPs-aPDL1 (green color) and PbS-aCD8 (red color) in the whole body. Scale bar: 5 mm. Similar results for n > 3 independent experiments.
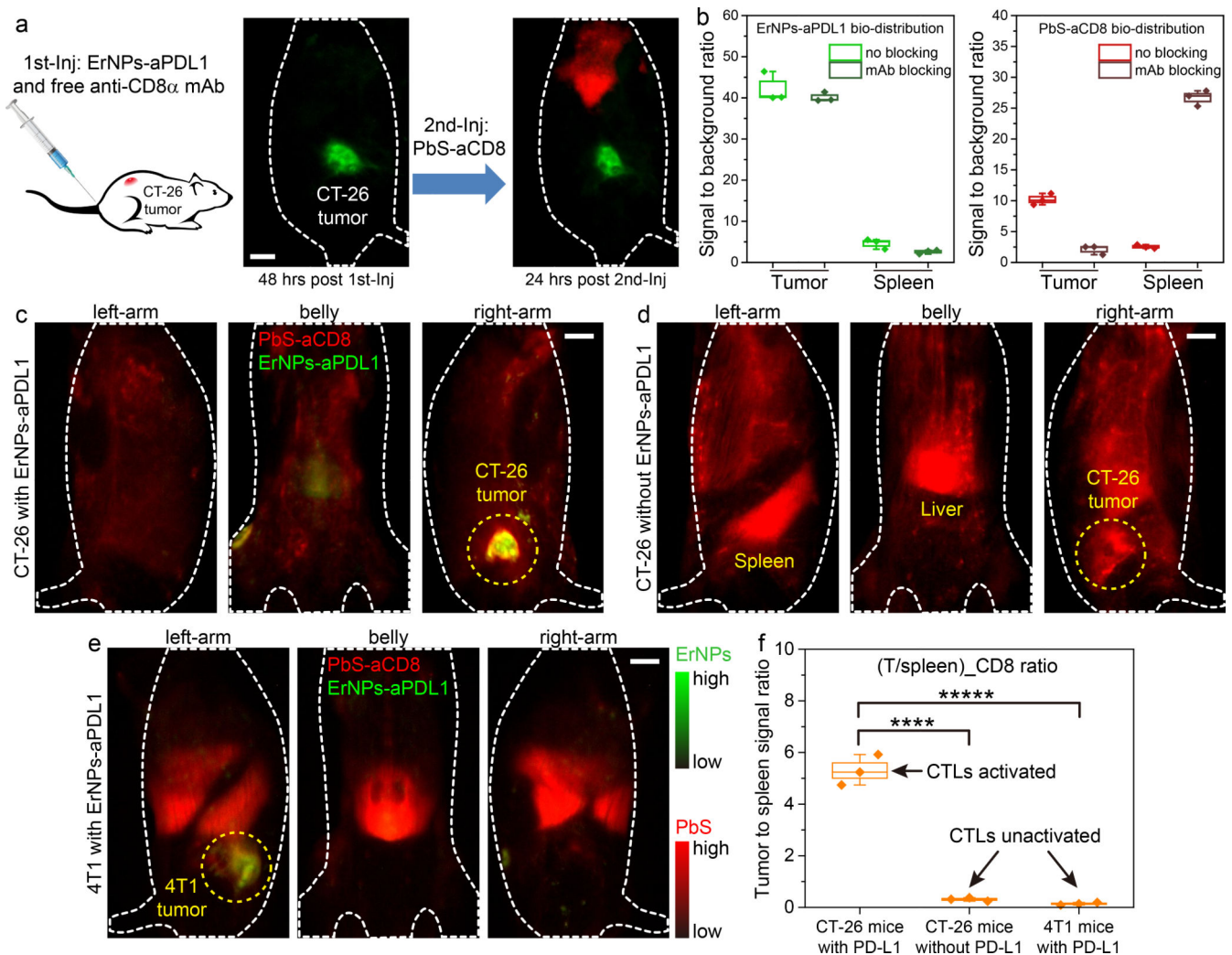
Figure 5: *In vivo* two-plex NIR-IIb molecular imaging of PDL1 and CD8+ CTLs for assessing immune activation and responses.

a, Schematic of the CD8α blocking experiment. A CT-26 tumor mouse was first intravenously injected with mixed ErNPs-aPDL1 and free anti-CD8α mAb (left wide-field image, 48 hrs post first injection), followed by a second intravenous injection of PbS-aCD8 (right wide-field image, 24 hrs post second injection). **b,** The signal of tumor and spleen to background ratios were plotted to reveal the bio-distribution of ErNPs-aPDL1 (left) and PbS-aCD8 (right) with CD8 and no blocking (mice n = 3 for each group). **c-e,** Wide-field images of mice from different directions (left-arm, belly, and right-arm) revealed the *in vivo* bio-distribution of ErNPs-aPDL1 and PbS-aCD8 in (**c**) a CT-26 tumor mouse intravenously injected with mixed ErNPs-aPDL1 and PbS-aCD8, (**d**) a CT-26 tumor mouse intravenously injected with only PbS-aCD8, and (**e**) a 4T1 tumor mouse intravenously injected with mixed ErNPs-aPDL1 and PbS-aCD8, at 24 hrs post injection. **f,** Corresponding (T/spleen)_CD8 ratios in these mice (n = 3 for each group). Green color: ErNPs-aPDL1 and red color: PbS-aCD8 for all these images. All data are presented as means ± s.d. All the scale bar is 5 mm. Data in **b**, **f** is presented as box plots (center line, median; box limits, upper and lower

quartiles; whiskers, 1.5x interquartile range; points, outliers). (****P = 0.0001, t = 14.4971, df = 4); (*****P = 0.0001, t = 15.0393, df = 4).

Table 1

Comparison of current NIR-IIb fluorescence/luminescence probes

	Required *in vivo* imaging exposure time (ms)	*In vivo* imaging frame rates (fps)	Excitation power (mW/cm^2)	Constituent elements	Excretion	Emission life-time (μs)^c
PbS QDs[9]	2–5	30–60	60–70	Pb^a, Cd^a, S	~ 76% within 28 days	46
InAs QDs[11]	5000	0.2	60	In, As^a, Cd^a, Se, S	--^{b}	~ 0.12
CNTs[8, 10]	200	4.6	150	C	Un-excretable	--^{b}
β-ErNPs[7, 43]	50–1000	3	100–140	Na, F, Yb, Y, Er	--^{b}	--^{b}
Ce-doped *β*-ErNPs[34]	20	25	150	Na, F, Yb, Y, Er, Ce	--^{b}	--^{b}
α-ErNPs (this work)	1.11–23.3	30–90	15–100	Na, F, Yb, Y, Er, Ce, Zn	~ 90% within 14 days	4300

^{a}Class I toxic metals defined by United States Pharmacopeia (USP).

^{b}No data provided.

^{c}Long emission lifetime can be utilized for multiplexed imaging.